RSC Advances

PAPER

View Article Online
View Journal | View Issue

Cite this: *RSC Adv.*, 2025, **15**, 24851

One-step co-precipitation synthesis, characterization, and enhanced photocatalytic performance of CaO/TiO_2-supported γ-Al_2O_3 nanocomposites (NCs) in wastewater treatment

Emaan Alsubhe *

Hybrid nanocomposites (NCs) have garnered significant attention for their potential applications, including photocatalysis, energy storage, and gas-sensing. This study reports the preparation, characterization, and photocatalytic activity of calcium oxide/titanium dioxide/gamma alumina (CaO/TiO_2/γ-Al_2O_3) NCs fabricated through a one-step co-precipitation processes. Different analytical tools, including X-ray diffraction (XRD), transmission electron microscopy (TEM), scanning electron microscopy (SEM) with energy dispersive X-ray spectroscopy (EDX), Raman spectroscopy, Fourier transform infrared spectroscopy (FTIR), photoluminescence spectroscopy (PL), ultraviolet-visible spectroscopy (UV-Vis), and dynamic light scattering (DLS), were carefully applied to examine the structural, morphological, and optical properties of the obtained NPs and NCs. The XRD results exhibited an important improvement in the crystallinity and phase purity of γ-Al_2O_3 NPs with supporting CaO NPs and TiO_2 NPs. TEM and SEM analyses verified that the synthesized NPs and NCs have a spherical morphology with a decrease in particle size from 9.50 $\pm$ 1.2 nm to 8.21 $\pm$ 2.1 nm after the addition of CaO NPs. EDX analysis revealed the presence of the elements calcium, titanium, aluminum and oxygen (Ca, Ti, Al, and O) within the CaO/TiO_2/γ-Al_2O_3 NCs. Raman and FTIR spectra determined the functional groups of the prepared samples. The reduction of the PL intensity indicates that the recombination of the electron–hole pairs is decreased upon adding CaO NPs and TiO_2 NPs. DLS results showed the surface charge and particle distribution of the synthesized NPs and NCs. The degradation of methylene blue (MB) dye under ultraviolet UV irradiation for 200 min was employed to examine the photocatalytic activity of these samples. As shown in the results, the photocatalytic activity of γ-Al_2O_3 NPs, TiO_2/γ-Al_2O_3 NCs, and CaO/TiO_2/γ-Al_2O_3 NCs reached up to 45%, 79%, and 98%, respectively. It can be observed that the CaO/TiO_2/γ-Al_2O_3 NCs achieved higher degradation than the individual samples. These improvements in the observed photocatalytic performance can be linked to various parameters, including the charge separation and increased surface area. The incorporation of CaO and TiO_2 into γ-Al_2O_3 enhances its photocatalytic efficiency by improving charge separation and expanding the surface area. They also promote light absorption and surface reactivity, which help suppress and increase the number of available active sites. These results highlight that the CaO/TiO_2/γ-Al_2O_3 NCs can enhance photocatalytic performance, especially the degradation of organic pollutants in wastewater. This study is an important step toward further research to apply these NCs in medical therapy.

Received 18th May 2025
Accepted 27th June 2025

DOI: 10.1039/d5ra03493k

rsc.li/rsc-advances

1. Introduction

Environmental technologies have drawn much attention to photocatalysis, which is a promising approach for degrading organic pollutants.[1,2] The current elimination of emerging contaminants, such as pollutant dyes, and antibiotics, in rivers, lakes, and seas remains a challenge for wastewater treatment processes.[3–5] However, the serious environmental problem of organic pollutants in water bodies has attracted and driven significant research studies toward finding efficient and sustainable methods to eliminate these pollutants using nanomaterials in different forms.[6,7] Among these nanomaterials, γ-Al_2O_3 nanoparticles (NPs) have been widely studied as one approach in wastewater treatment processes owing to their superior physicochemical properties, such as good stability and excellent photocatalysis efficiency under UV and visible irradiation.[8,9] Nevertheless, it has many limitations, such

Department of Physics, College of Science, Taibah University, Yanbu 46423, Saudi Arabia. E-mail: esobhe@taibahu.edu.sa

as a wide band gap (~3.6 eV), which plays a role in decreasing its photocatalytic activity due to a high rate of recombination of pairs (electrons (e^-) and holes (h^+)).[10] To address these limitations, different approaches have been applied to improve its photocatalytic activity, including coupling with other metal oxide nanoparticles (NPs) or doping with metal ions to create a new nanocomposite.[11,12] Moreover, the γ-Al_2O_3 NP mixtures support different metal oxide NPs, such as ZnO,[13] ZrO_2,[14] TiO_2,[15] CaO,[16] CuO,[17] and SnO_2 NPs,[18] which have attracted increasing interest because of their exceptional properties, including high surface area and strong stability.

To optimize the photocatalytic properties of the hybrid metal oxide NCs, synthesis plays a crucial role. Likewise, chemical, physical, and biological techniques have been widely developed to prepare hybrid metal oxide NPs like γ-Al_2O_3 NPs to enhance their potential applications. For example, Huang *et al.*[19] used the co-precipitation route to synthesize *N*-TiO_2/γ-Al_2O_3 nanostructures for improved photodegradation (92.5%) of 2,4-dichlorophenol dye under fluorescence irradiation (60 W). In another instance, the sol–gel process was applied to prepare Fe-doped TiO_2/γ-Al_2O_3 NCs with high photocatalytic activity compared with pure γ-Al_2O_3. Mahdi *et al.*[20] investigated the use of clove extract to prepare γ-Al_2O_3 NPs, revealing that they exhibited high antimicrobial activity and effective removal of metal ions from water. Dubadi *et al.*[21] reported that various metal oxide NPs, such as Fe_2O_3, CuO, ZnO, Bi_2O_3, and Ga_2O_3, have been combined with γ-Al_2O_3 using liquid-assisted grinding to synthesize nanocomposites (NCs) with high aromatic pollutant degradation. Moreover, Kudla *et al.*[22] prepared Zr and Mg-doped γ-Al_2O_3 NCs using hydrothermal treatment to enhance the thermal stability. The Cu, Pd, Ni, Co/γ-Al_2O_3 demonstrated high photodegradation of the methylene blue, 4-nitrophenol, nitrite, and nitrate dyes compared to pure γ-Al_2O_3.[23] In the past few years, as a result of their physicochemical characteristics, the enhancement of photocatalyst materials has attracted significant attention in potential applications. Furthermore, several studies reported that different oxide compounds of metal (*e.g.*, TiO_2, CuO, SnO_2, ZnO and NiO) have been combined with other metal oxide NPs to improve their photocatalytic performance in environmental remediation and wastewater treatment.[24,25] Kanwal *et al.*[26] have discovered that Mn_2O_3/γ-Al_2O_3 NCs exhibit better-quality photocatalytic activity compared with the pure components. As a result, the co-precipitation method provides a simple, cost-effective and scalable route to synthesize nanocomposites with controlled particle size, uniform composition and high purity, making it superior to other methods such as hydrothermal treatment and sol–gel synthesis for practical uses.[19,27]

The present work focuses on fabricating CaO/TiO_2/γ-Al_2O_3 as a catalyst for enhancing photocatalytic performances, particularly the degradation of organic contaminants. The chemical co-perception process was successfully applied to synthesize samples. The physicochemical properties of the prepared samples were investigated through analytical methods, including XRD, Raman, SEM with EDX, FTIR, PL, and DLS. The degradation of the methylene blue (MB) dye under UV light was used to investigate the photocatalytic efficiency of the catalysts.

2. Experimental part

2.1 Chemicals and methods

In these experiments, all chemical materials were utilized without further purification. Gamma-alumina (γ-Al_2O_3) (99.95% trace metals), titanium(IV) butoxide (Ti(O-But)$_4$), calcium nitrate ($Ca(NO_3)\cdot 4H_2O$), sodium hydroxide (NaOH), and methylene blue (MB) dye were supplied from Sigma-Aldrich Company (St. Louis, MO, USA). In all experiments, distilled water and ethanol were employed as solvents.

2.2 Preparation of CaO/TiO_2/γ-Al_2O_3 NCs

The chemical co-precipitation process was successfully applied to prepare CaO/TiO_2/γ-Al_2O_3 (15 : 15 : 70) nanocomposites (NCs) using the following procedures as a one-step method. Firstly, 0.07 mol of γ-Al_2O_3 NPs was added to 30 mL of water and a magnetic stirrer in a 250 mL round-bottomed flask. Next, 0.015 mol of Ti(O-But)$_4$ was mixed with 10 mL of ethanol and added to the above solution under stirring. After that, 0.015 mol of $Ca(NO_3)\cdot 4H_2O$ was mixed with the prior solution, followed by stirring for 1 h. Then, 0.031 mol of NaOH in 15 ml water was slowly added to the mixture solution with stirring at 65 °C for 5 h. Following filtration, the sample was repeatedly washed with ethanol and water, then dried in the oven at 60 °C for 24 h. The dried powder was calcined at 500 °C under air for 4 h to produce CaO/TiO_2/γ-Al_2O_3 NCs. By applying the same procedures, TiO_2/γ-Al_2O_3 NCs (30 : 70) were further produced with amount of γ-Al_2O_3 (0.1 mol) and Ti(O-But)$_4$ (0.03 mol), and without $Ca(NO_3)\cdot 4H_2O$.

2.3 Characterization tools

Several analytical techniques were used to investigate the enhanced physicochemical properties. X-ray diffraction (XRD) analysis (AXRD Benchtop, Proto Manufacturing, Inc., USA) was used to examine the crystalline and phase purity properties. The surface morphology, structure, particle size, and elemental compositions of the synthesized samples were further examined *via* transmission electron microscopy (TEM) (JEM-2100F, JEOL, Inc., Tokyo, Japan) and scanning electron microscopy (SEM) (JSM-7600F, JEOL, Inc., Tokyo, Japan) with energy-dispersive X-ray spectroscopy (EDX) techniques. Raman spectroscopy (STR 500 Confocal Micro Raman spectrometer) was used to assess the crystal structure of the prepared samples. Likewise, FTIR spectroscopy (PerkinElmer Paragon 500, USA) was used to determine the functional groups of the synthesized samples. PL spectroscopy (Hitachi F-4600) was applied to study the optical properties. The surface charges and particle distribution of the samples were evaluated through dynamic light scattering (DLS) (Malvern, Worcestershire, UK).

2.4 Photocatalytic experiments

We used methyl blue (MB) dye to evaluate the γ-Al_2O_3 NPs, TiO_2/γ-Al_2O_3 NCs, and CaO/TiO_2/γ-Al_2O_3 NCs as catalysts. Initially, 10 ppm of the MB solution was mixed with 40 mg of each catalyst. Then, the mixed solution was placed under dark

conditions with magnetic stirring for 30 minutes to test the absorption–adsorption equilibrium. After that, it was irradiated with a UV light source for 200 minutes. After being exposed for 20 minutes, a micropipette was used to take 3.0 mL of the mixture solution. The sample was centrifuged at 4000 rpm for 10 minutes to remove it from the dye solution. Subsequently, the absorbance of the MB solution was measured using UV-Vis spectroscopy. The dye degradation efficiency was measured using the following eqn (1):

$$\text{Degradation efficiency } (\%) = [(C_0 - C_t)/C_0] \times 100 \quad (1)$$

where C_0 is the first absorbance of the MB dye without samples, and C_t is the absorbance at a specific exposure time (t). The constant rate (K) of the MB degradation was calculated using eqn (2) as follows:

$$K_t = \ln [C_0/C_t] \quad (2)$$

where K is the constant rate of degradation, C_0 is the first absorbance of the MB dye without samples, and C_t is the absorbance at exposure time (t). Under the same experimental conditions, cyclic photocatalysis tests were performed using $CaO/TiO_2/\gamma$-Al_2O_3 NCs. After dark adsorption, a 200 min photocatalytic decomposition of MB was applied, and the process was repeated four times. After each cycle, the photocatalyst was separated from the MB solution by centrifugation and washed three times with ethanol. The powder was then dried at 60 °C for 24 h before being reused.

3. Results and discussions

3.1 XRD study

XRD analysis was performed to investigate the crystallinity and phase composition of the prepared samples. Fig. 1 depicts the XRD pattern of the produced γ-Al_2O_3 NPs, TiO_2/γ-Al_2O_3 NPs, and $CaO/TiO_2/\gamma$-Al_2O_3 NPs. In Fig. 1a, the observed peaks of the γ-Al_2O_3 NPs were at 2θ = 32° (220), 37° (311), 39° (222), 46° (400), 61° (511), and 67° (440). These peaks confirm the structure of γ-Al_2O_3, as demonstrated in previous studies.[28,29] In the analysis of the TiO_2/γ-Al_2O NCs (Fig. 1b), several new peaks were detected at 2θ = 25° (101), 47° (200), 55° (105), 63° (204) and assigned to TiO_2, similar to earlier studies.[30–32] Additionally, peaks corresponding to the presence of γ-Al_2O_3 were observed. These findings confirm the successful combination of TiO_2–Al_2O_3 NCs. In contrast, the XRD spectra of $CaO/TiO_2/\gamma$-Al_2O_3 NCs (Fig. 1c) exhibited sharp peaks compared to those of both γ-Al_2O_3 NPs and TiO_2/γ-Al_2O_3 NCs, indicating a higher degree of crystallinity in the $CaO/TiO_2/\gamma$-Al_2O_3 NCs. Significantly, new peaks appeared at 31° (111), 44° (200), 44° (220) and 50° (220), which agrees with previous studies of CaO.[33–35] Additionally, the peaks at 25°, 37°, 45° and 67° confirm the synthesis of $CaO/TiO_2/\gamma$-Al_2O_3 NCs. The average crystalline size at 67° (440) for all synthesized samples were calculated by Scherrer's eqn (3), which is given as follows:[28]

$$\text{Crystallite size } (D) = \frac{K\lambda}{\beta \cos \theta} \quad (3)$$

where D is the crystallite size (in nanometers), and K is the shape factor (0.9). λ is the X-ray wavelength (Cu-Kα radiation, λ = 1.5406 Å), β is the full width at half maximum (FWHM) of the diffraction peak in radians, and θ is the diffraction angle (in radians). It can be observed that the average crystallinity size of the prepared γ-Al_2O_3 NPs, TiO_2/γ-Al_2O_3 NCs, and $CaO/TiO_2/\gamma$-Al_2O_3 NCs were 3.2 ± 1.4 nm, 2.4 ± 0.8 nm, and 2.7 ± 0.5 nm, respectively, as illustrated in Table 1. These values indicate that the addition of TiO_2 and CaO played a role in enhancing the crystal structure. The XRD spectra confirmed that $CaO/TiO_2/\gamma$-Al_2O_3 NCs could be applied in potential applications, such as photocatalysis, gas-sensing, and energy storage. The obtained XRD results were in good agreement with earlier investigations.[29,31,33]

3.2 TEM analysis

Fig. 2a–i displays the TEM images, HRTEM images, and the particle size for Al_2O_3 NPs, TiO_2/γ-Al_2O_3 NCs, and $CaO/TiO_2/\gamma$-Al_2O_3 NCs. As illustrated in Fig. 2a and c, the TEM image of the pure γ-Al_2O_3 NPs was found to be spherical in shape with an average particle size of 9.55 ± 1.2 nm, similar to previous studies.[36,37] Fig. 2b shows that the d-spacing of γ-Al_2O_3 NPs was 0.238 nm, which matched with the XRD data (Fig. 1a). For TiO_2/γ-Al_2O_3 NCs (Fig. 2d–f), the particle size of NCs has a spherical shape with a decreased size (7.60 ± 0.9 nm) compared with pure γ-Al_2O_3 NPs. The decrease in particle size is likely due to the interaction of TiO_2 with the surface of γ-Al_2O_3, stabilizing smaller particles and preventing their agglomeration.[38,39] It was observed that the d-spacing values for TiO_2/γ-Al_2O_3 were 0.193 nm and 0.321 nm for γ-Al_2O_3 NPs and TiO_2, respectively.[40,41] These values indicate that TiO_2/γ-Al_2O_3 NCs were successfully prepared. Additionally, Fig. 2g shows the TEM image of the prepared $CaO/TiO_2/\gamma$-Al_2O_3 NCs. As a result, the particles of γ-Al_2O_3 NPs exhibited more agglomeration with increased size (8.21 ± 2.1 nm) after the addition of the CaO compared to an individual sample, as shown in Table 1. Recent studies have reported that the crystallinity refers to the degree of order or regularity in the arrangement of atoms within a material, while the particle size (or crystallite size) refers to the physical size of the individual crystalline domains.[42,43] As observed in the XRD data, the crystallites of the $CaO/TiO_2/\gamma$-Al_2O_3 NCs are smaller (2.7 nm) compared to the γ-Al_2O_3 NPs and TiO_2/γ-Al_2O_3 NCs. This indicates that the CaO addition leads to smaller, yet well-ordered crystalline domains. Fig. 2i demonstrates the d-spacing of the structure, which was 0.235 nm, 0.312 nm, and 0.241 nm for γ-Al_2O_3 NPs, TiO_2 NPs and CaO NPs, respectively. The TEM results were in good agreement with earlier studies,[9,39,44] and matched well with the XRD data (Fig. 1a–c).

3.3 SEM with EDX analysis

The SEM and EDX analyses was performed on the fabricated samples to study their surface morphology properties, as illustrated (Fig. 3a–d). It can be observed in Fig. 3a that the pure γ-Al_2O_3 NPs have a spherical shape with less agglomerations. As illustrated in Fig. 3a–c, the structural morphologies of the

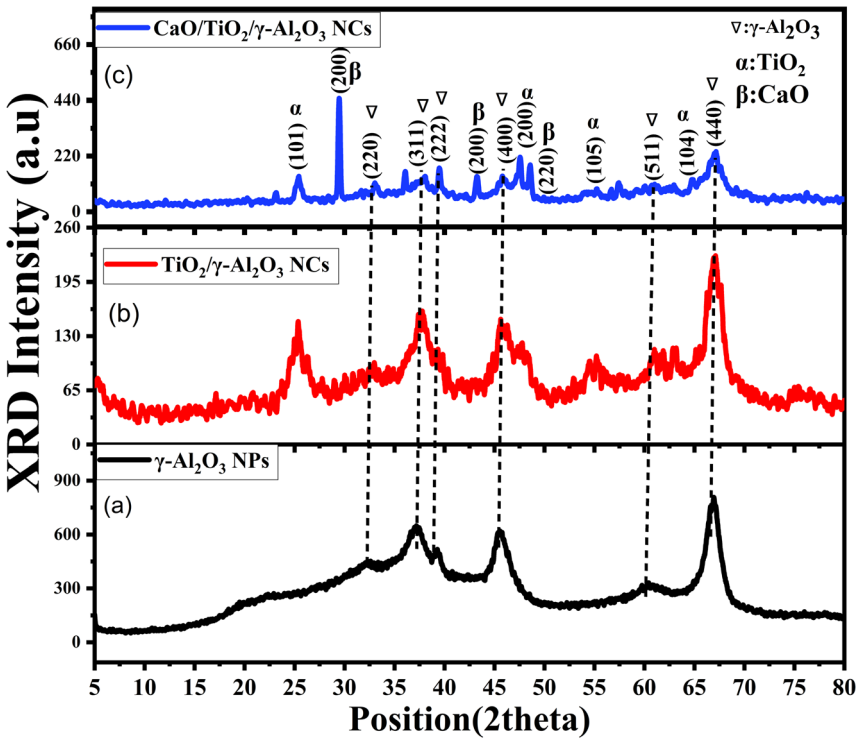

Fig. 1 XRD pattern: (a) γ-Al_2O_3 NPs, (b) TiO_2/γ-Al_2O_3 NCs, and (c) CaO/TiO_2/γ-Al_2O_3 NCs.

Table 1 Structural properties of synthesized metal oxide NPs and NCs

Catalyst used	TEM (nm)	XRD (nm)
γ-Al_2O_3 NPs	9.55 ± 1.2 nm	3.2 ± 1.4
TiO_2/γ-Al_2O_3 NCs	7.60 ± 0.9 nm	2.4 ± 0.8
CaO/TiO_2/γ-Al_2O_3 NCs	8.21 ± 2.1	2.7 ± 0.5

prepared samples were irregular in shape with more agglomeration, which might point to the combination of CaO and TiO_2 into γ-Al_2O_3 NPs. These results are also in line with previous studies.[9,45] Fig. 3a–c illustrates the presence of porosity, which is considered one of the significant characteristics for photocatalyst activity. As shown by previous research studies, it increases the surface area, which plays a vital role in enhancing the catalytic performance. In addition, the stability and reusability of the catalysts can be enhanced by porosity.[46,47] Furthermore, Fig. 3d presents the EDX spectra that reveal the presence of Ca, O, Ti and Al in the synthesized CaO/TiO_2/γ-Al_2O_3 NCs, reflecting the formation of CaO/TiO_2/γ-Al_2O_3 NCs. The presented SEM images were in good agreement with the TEM results (Fig. 2).

3.4 FTIR analysis

FTIR analysis of the calcined γ-Al_2O_3 NPs, TiO_2–Al_2O_3 NCs, and CaO/TiO_2/γ-Al_2O_3 NCs at 500 °C was carried out. Fig. 1 shows the FTIR pattern of synthesized NPs and NCs. It can be seen in the FITR of γ-Al_2O_3 NPs and TiO_2/Al_2O_3 NCs that the bands observed at around 3449.8 cm^{-1} assigned to the O–H stretching bands indicate the occurrence of surface hydroxyl groups or adsorbed moisture. This peak is usually broad due to hydrogen bonding between the hydroxyl groups, as reported in many previous studies.[45,48] Similarly, the bands around 1628.6 cm^{-1} can be attributed to O–H bending vibrations. Furthermore, the bands at 550–800 cm^{-1} are associated with the vibrational stretching modes of the Al–O, Ti–O, and Ca–O bonds in the oxide lattice. Importantly, the FTIR spectra of CaO/TiO_2/γ-Al_2O_3 showed similar absorption bands corresponding to hydroxyl groups (O–H stretching at 3434.59 cm^{-1}). Peaks were observed at 1389.3 cm^{-1}, indicating the presence of calcium carbonate due to the reaction with CO_2. The FTIR spectra of CaO–TiO_2-γ-Al_2O_3 NCs show a strong basic property at 1500 cm^{-1}, which can be linked to the absorption of CO_2 from the atmosphere. This indicates the alteration of CaO and TiO into γ-Al_2O_3. Our FTIR results were in agreement with earlier studies.[29,45,48]

3.5 Raman analysis

The Raman pattern of the calcined γ-Al_2O_3 NPs, TiO_2/γ-Al_2O_3 NCs, and CaO/TiO_2/γ-Al_2O_3 NCs are presented in Fig. 5. As observed, the γ-Al_2O_3 NPs display peaks at around 276.5 cm^{-1}, which is attributed to the O–Al–O bending mode. Furthermore, peaks at around 563.5 cm^{-1} and 695.1 cm^{-1} are determined to be Al–O stretching, in accordance with the formation of γ-Al_2O_3 NPs.[49] Moreover, the Raman spectra of TiO_2/γ-Al_2O_3 NCs exhibited new peaks at 145.6 cm^{-1}, 563.5 cm^{-1}, and 691 cm^{-1}, as a similar reported study.[50] The Raman shifts demonstrate the interactions at the interface of TiO_2 and γ-Al_2O_3. Additionally, peaks at 1095.1 cm^{-1} and 2418.8 cm^{-1} could be caused by the stretching vibration of O–H. Likewise, CaO/TiO_2/γ-Al_2O_3 NCs present peaks at 145.6 cm^{-1},276.5 cm^{-1},

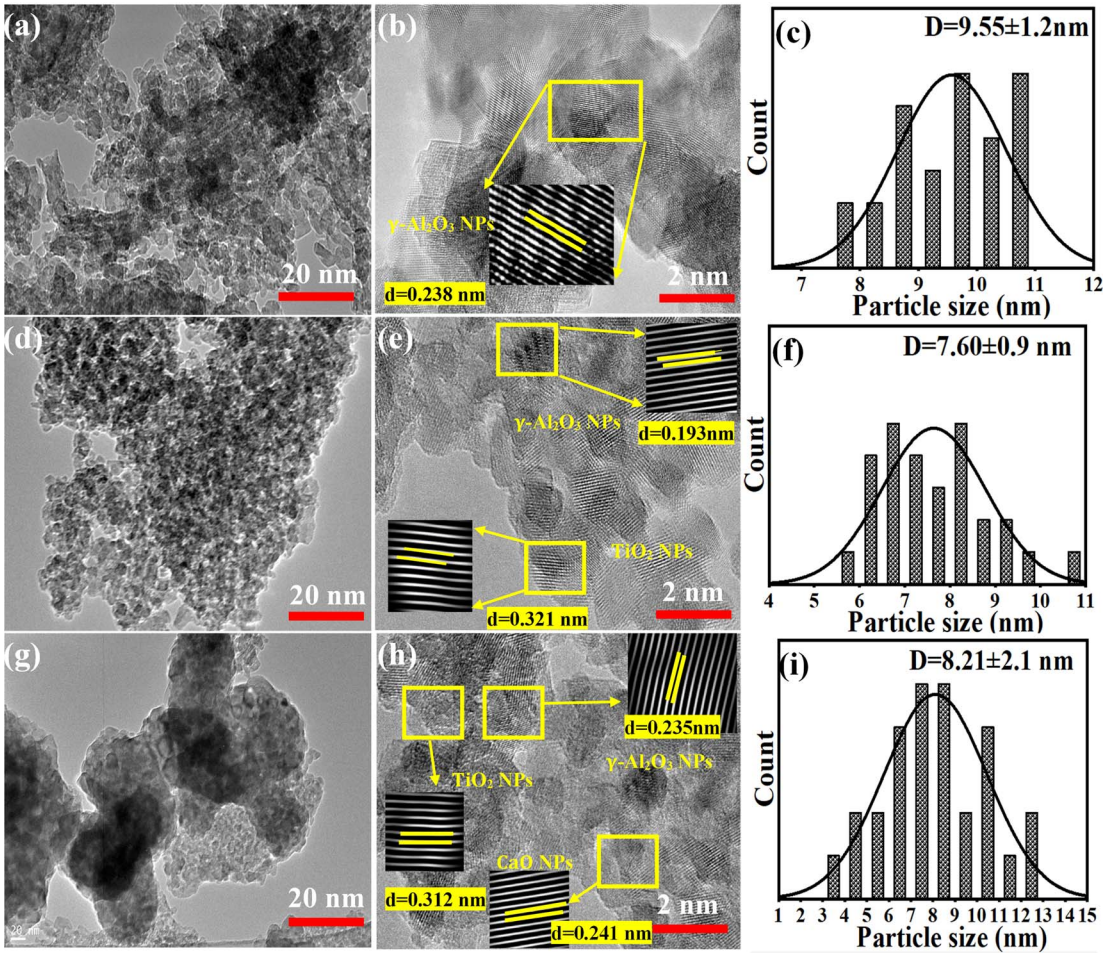

Fig. 2 TEM and HRTEM images, and particle size: (a–c) pure γ-Al_2O_3 NPs, (d–f) TiO_2/γ-Al_2O_3 NPs, and (g–i) CaO/TiO_2/γ-Al_2O_3 NCs.

563.5 cm^{-1},691 cm^{-1},784.3 cm^{-1}, 1095.1 cm^{-1} and 2429 cm^{-1}. The primary Raman active mode of CaO is detected at around 710 cm^{-1}, arising from the stretching vibrations of the Ca–O bond.[51] Nevertheless, the high peak intensities could be attributed to the crystallinity quality of CaO/TiO_2/γ-Al_2O_3 NCs. The combined spectrum allows for the identification of all three components, verifying the successful synthesis of the NPs and NCs. These results agreed with the FTIR data (Fig. 4).

3.6 UV-Vis and PL study

The UV-vis absorption spectra of γ-Al_2O_3 NPs, TiO_2/γ-Al_2O_3 NCs and CaO/TiO_2/γ-Al_2O_3 NCs are presented in Fig. 6a. An absorption peak at 380 nm was recorded, indicating the formation of γ-Al_2O_3 NPs, which is in good agreement with recent studies.[52,53] CaO/TiO_2/γ-Al_2O_3 NCs exhibited higher absorption intensity compared to both γ-Al_2O_3 NPs and TiO_2/γ-Al_2O_3 NCs, demonstrating superior photocatalytic performance under UV irradiation. From the absorption spectra, the optical band gap energies were estimated to be 3.30 eV, 3.00 eV and 3.73 eV for γ-Al_2O_3 NPs, TiO_2/γ-Al_2O_3 NCs, and CaO/TiO_2/γ-Al_2O_3 NCs, respectively.

In addition, PL analysis was performed for γ-Al_2O_3 NPs, TiO_2/γ-Al_2O_3 NCs, and CaO/TiO_2/γ-Al_2O_3 NCs to understand the electronic and optical properties at an excitation wavelength of 355 nm. As shown in Fig. 6b, the higher intensity for γ-Al_2O_3 NPs occurred at 406.2 nm with band-to-band transitions, in agreement with earlier studies.[54,55] Shoulder peaks occurred at 425.1 nm and 477.9 nm, which could be linked to oxygen vacancies or aluminum-related defects. The peak that appeared at 523.5 nm could be related to transitions involving defect states. However, the intensity of the peaks of TiO_2/γ-Al_2O_3 NCs was higher than those of γ-Al_2O_3 NPs. Similarly, TiO_2/γ-Al_2O_3 and CaO/TiO_2/γ-Al_2O_3 NCs exhibited the same peaks of γ-Al_2O_3 NPs. However, the intensity was higher than γ-Al_2O_3 NPs and TiO_2/γ-Al_2O_3 NCs.[32] Furthermore, the peak at 523.5 nm of TiO_2/γ-Al_2O_3 NCs might be bound to Ti^{+3} ions.[56] These finding shows that the composite with CaO and TiO_2 improves the PL properties of γ-Al_2O_3 NPs, making it beneficial for catalyst applications.

3.7 Zeta potential analysis

Dynamic light scattering (DLS) determines the particle distribution, surface charge, and stability of synthesized samples. Fig. 7a shows the particle distribution of the synthesized samples. It can be observed that the average particle distribution of the synthesized γ-Al_2O_3 NPs, TiO_2/γ-Al_2O_3 NPs, and CaO/TiO_2/γ-Al_2O_3 NCs were found to be 190.2 ± 68.1 nm, 180.5 ± 90.3 nm, and 188.2 ±

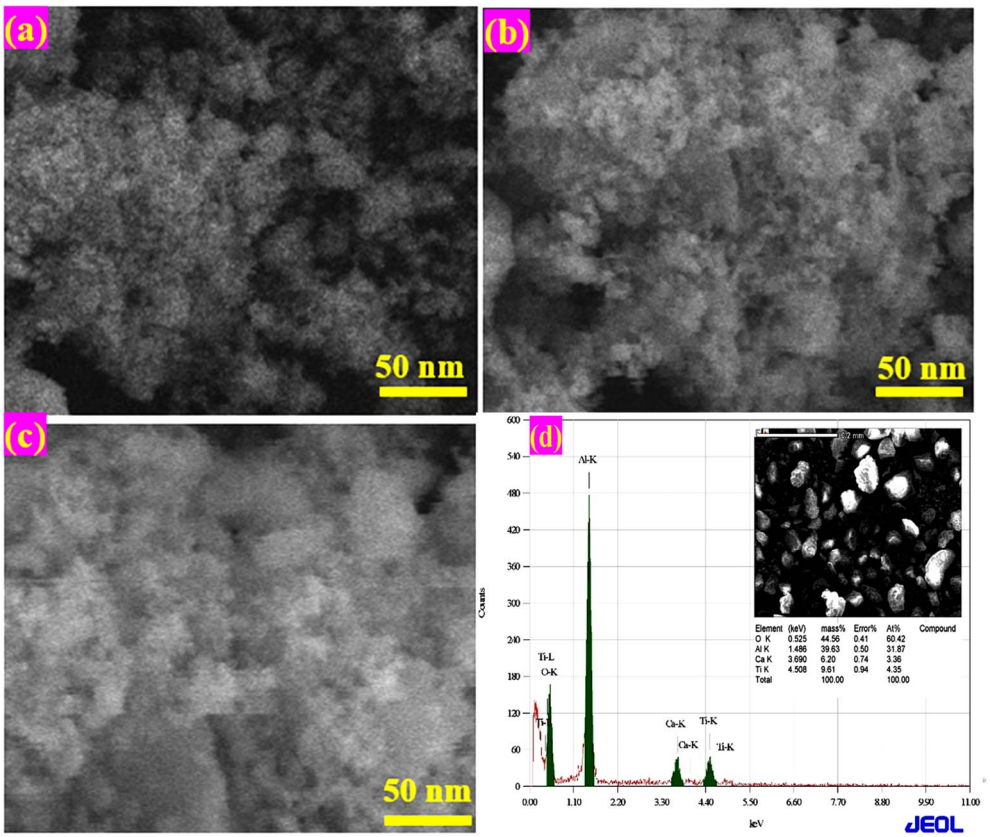

Fig. 3 SEM Analysis: (a) SEM image of γ-Al_2O_3 NPs, (b) TiO_2/γ-Al_2O_3 NPs, (c) CaO/TiO_2/γ-Al_2O_3 NCs. (d) EDX spectra of CaO/TiO_2/γ-Al_2O_3 NCs.

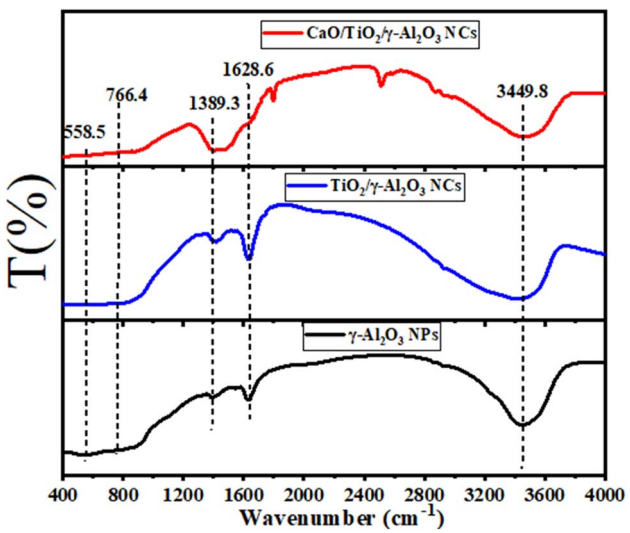

Fig. 4 FTIR spectra of γ-Al_2O_3 NPs, TiO_2/γ-Al_2O_3 NCs, and CaO/TiO_2/γ-Al_2O_3 NCs.

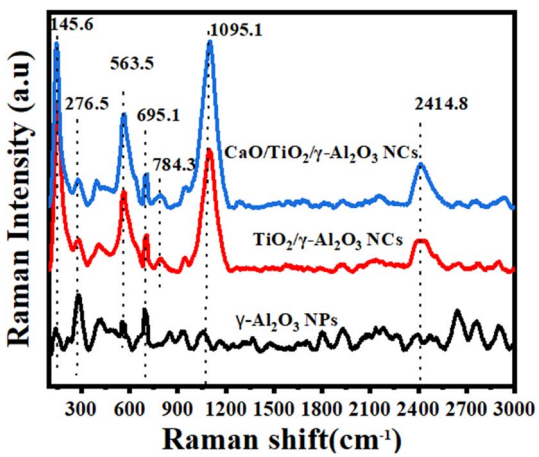

Fig. 5 Raman spectra of γ-Al_2O_3 NPs, TiO_2/γ-Al_2O_3 NCs, and CaO/TiO_2/γ-Al_2O_3 NCs.

75.0 nm, respectively, as shown in Table 2. These results were supported by TEM data (Fig. 2). Moreover, the surface charge was measured to evaluate the stability of the three samples, which is critical for catalytic applications. The zeta potential of γ-Al_2O_3 is highly pH-dependent due to the ionization of the surface hydroxyl groups. As represented in Fig. 4a, the zeta potential value of γ-Al_2O_3 NPs was found to be -11.2 ± 16.6 mV, which could define the amorphous phase of γ-Al_2O_3 NPs.[57] This zeta potential result might also be correlated with the aggregation of the sample during synthesis. In contrast, the zeta potential of TiO_2/γ-Al_2O_3 NCs was -26.5 ± 6.5 mV, indicating better stability than γ-Al_2O_3 NPs (Fig. 4b).[44] Furthermore, the zeta potential of CaO/TiO_2/γ-Al_2O_3 nanocomposites (NCs) was -28.9 ± 4.3 mV, signifying a high surface charge due to the incorporation of CaO, as

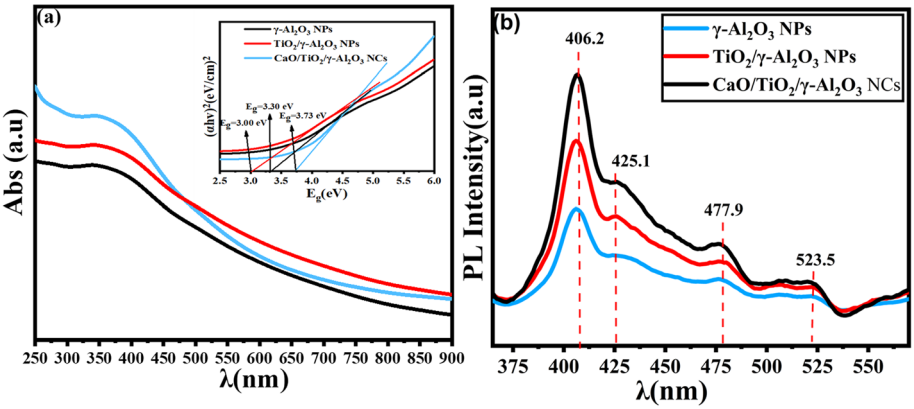

Fig. 6 (a) UV-Vis pattern and (b) PL pattern of the prepared γ-Al_2O_3 NPs, TiO_2/γ-Al_2O_3 NCs, and CaO/TiO_2/γ-Al_2O_3 NCs.

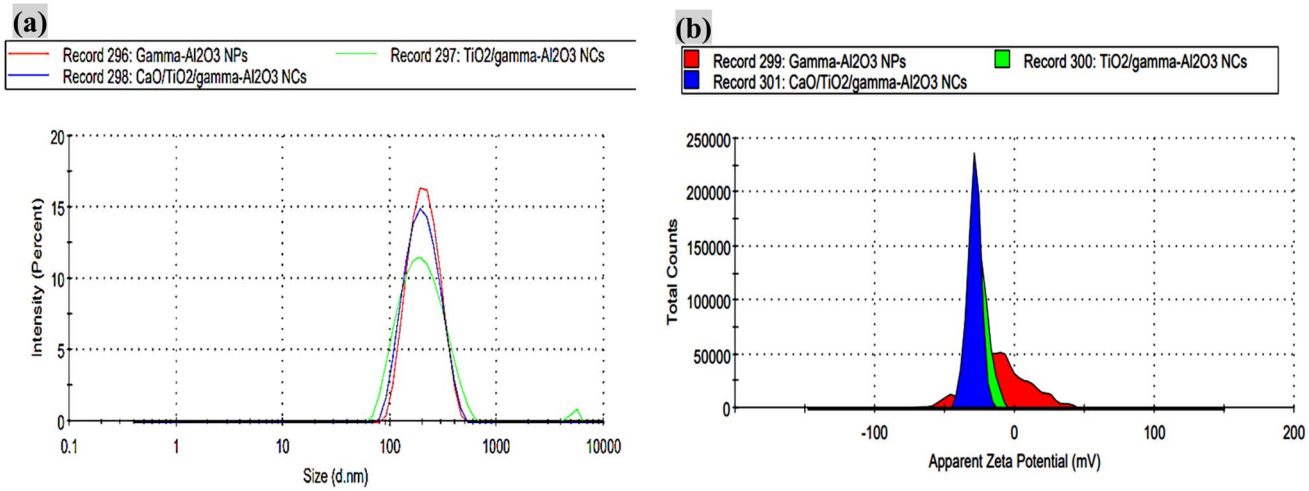

Fig. 7 (a) Particle distribution and (b) zeta potential analysis for the prepared γ-Al_2O_3 NPs, TiO_2/γ-Al_2O_3 NCs, and CaO/TiO_2/γ-Al_2O_3 NCs.

illustrated in Fig. 4c. Understanding the zeta potential of the NP and NCs samples is fundamental for their application in catalysis, adsorption processes, and as support materials in heterogeneous catalysis, as it impacts the particle dispersion and reactivity.

3.8 Photocatalytic evaluation

The photocatalysis studies of the MB dye using pure γ-Al_2O_3 NPs, TiO_2/γ-Al_2O_3 NCs, and CaO/TiO_2/γ-Al_2O_3 NCs were carried out under direct UV light for 200 min (Fig. 8a–f). As can be observed in Fig. 8a, the UV absorption of γ-Al_2O_3 NPs decreased with increasing exposure time. Moreover, a notable reduction of the UV absorption was achieved for TiO_2/γ-Al_2O_3 NCs for a duration of 200 min (Fig. 8b). Additionally, a significant decrease in the UV absorption of CaO/TiO_2/γ-Al_2O_3 NCs was detected with an expansion in the duration time (Fig. 8c). This observation of CaO/TiO_2/γ-Al_2O_3 NCs signifies the essential impact of the sample in breaking down organic pollutants. Correspondingly, Fig. 8e demonstrates the constant rates of 0.0027 min^{-1}, 0.0074 min^{-1} and 0.0140 min^{-1} for γ-Al_2O_3 NPs, TiO_2/γ-Al_2O_3 NCs and CaO/TiO_2/γ-Al_2O_3 NCs, respectively. As shown in the results, the high color of the MB solution was rapidly degraded with the CaO/TiO_2/γ-Al_2O_3 NCs compared to the individual samples. Moreover, Fig. 8f displays the degradation efficiency of the prepared samples, which was 45% for γ-Al_2O_3 NPs, 79% for TiO_2/γ-Al_2O_3 NCs, and 94.1% for CaO/TiO_2/γ-Al_2O_3 NCs, respectively. These values showed that the addition of CaO and TiO_2 into γ-Al_2O_3 plays a role in enhanced photocatalytic degradation (Table 3).

Table 2 Summary of the DLS data of the prepared γ-Al_2O_3 NPs, TiO_2/γ-Al_2O_3 NCs, and CaO/TiO_2/γ-Al_2O_3 NCs

Sample used	Particle size (nm ± SD)	Zeta potential (mV ± SD)
γ-Al_2O_3 NPs	190.2 ± 68.1	−11.2 ± 16.6
TiO_2/γ-Al_2O_3 NCs	180.5 ± 90.3	−26.5 ± 6.5
CaO/TiO_2/γ-Al_2O_3 NCs	188.2 ± 75.0	−28.9 ± 4.3

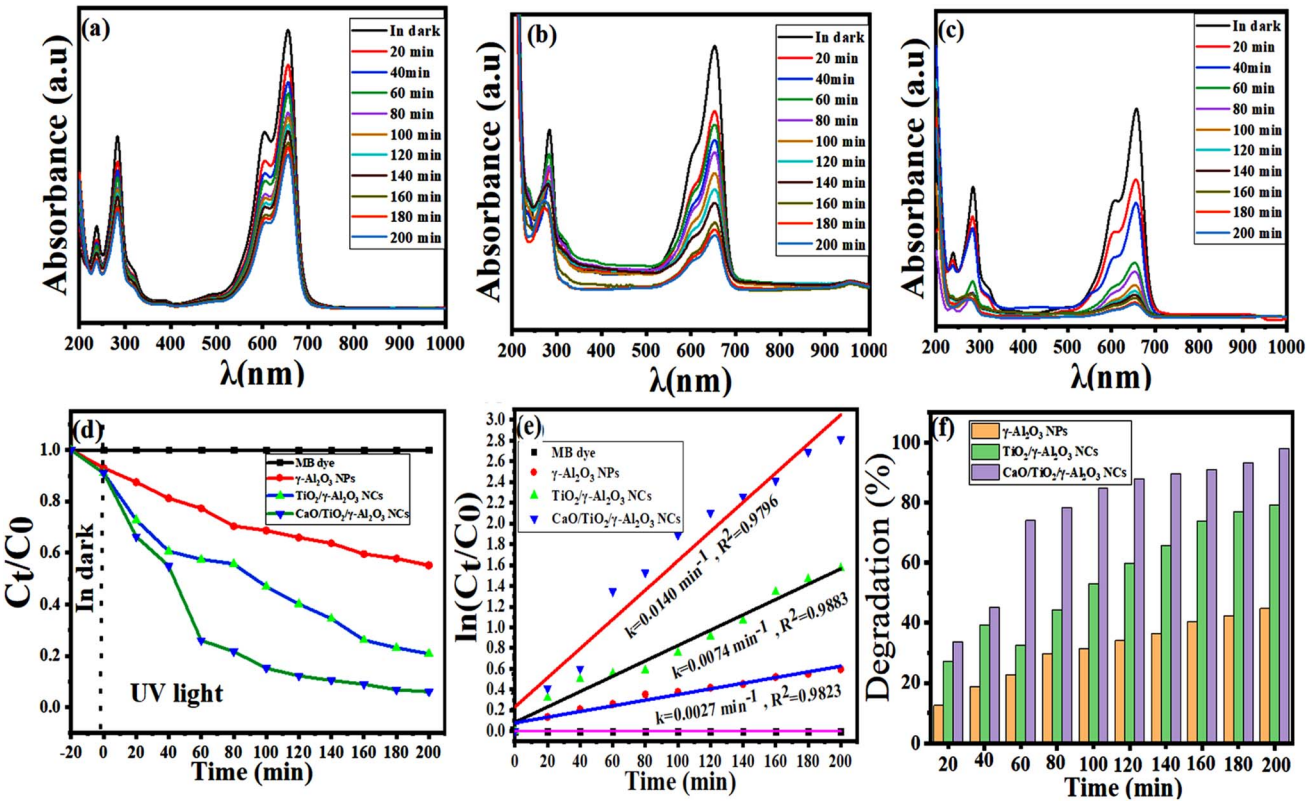

Fig. 8 (a–c) UV-Vis absorbance of the MB dye solution by γ-Al_2O_3 NPs, TiO_2/γ-Al_2O_3 NCs, and CaO/TiO_2/γ-Al_2O_3 NCs. (d) Plot of (C_t/C_0) *vs.* irradiation time (min), (e) kinetics of the photocatalysis of the MB solutions for the prepared samples, and (f) degradation efficiency (*D*%) of the MB solution using the synthesize d catalyst.

3.8.1 The recycling stability of the catalyst. In this investigation, the same CaO/TiO_2/γ-Al_2O_3 NCs were used to degrade MB dye under UV irradiation to evaluate its stability and the recycling potential of the photocatalysts. Without any additional processing, the CaO/TiO_2/γ-Al_2O_3 NCs were recycled four times under the same conditions using centrifugation. Fig. 9 shows the recycling stability of the prepared CaO/TiO_2/γ-Al_2O_3 NCs over four cycles of photocatalytic degradation. As observed in the results, the degradation efficiency remains high throughout the cycles, with only a slight decrease from 94.1% in the first cycle to 92.1% in the fourth cycle. This phenomenon demonstrates the excellent stability and reuse potential of the prepared NCs. This work suggests that the CaO/TiO_2/γ-Al_2O_3 nanocomposites (NCs) could be utilized in potential applications, such as environmental remediation and medical therapy.

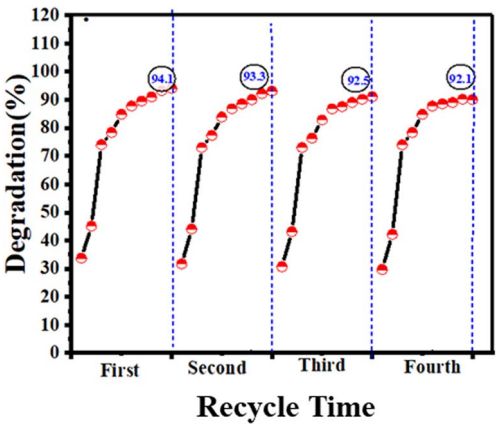

Fig. 9 Recycling stability of the synthesized CaO/TiO_2/γ-Al_2O_3 NCs.

Table 3 Comparison of the degradation efficiency between the presented samples and previous different samples

Sample used	Experimental conditions	Irradiation time (min)	Degradation target	Degradation efficiency (%)	Ref.
CaO/TiO_2/γ-Al_2O_3 NCs	UV light	200	MB	94.1%	This study
Au/BiOBr/graphene	Visible light	180	Phenol	64%	6
MgO/Fe_2O_3/γ-Al_2O_3 NCs	UV light	140	MB	90.4%	9
Mn–S co-doped TiO_2 NCs	Sun light	120	Phenol	59%	58
α-Fe_2O_3/ZnO NCs	UV light	120	MB	91.6%	59
CuO/MoS_2@gCN NCs	UV light	35	Phenol	63.50%	60
Nb(2.0)/TiO_2 nanocomposite	UV	160	Phenol	94%	61

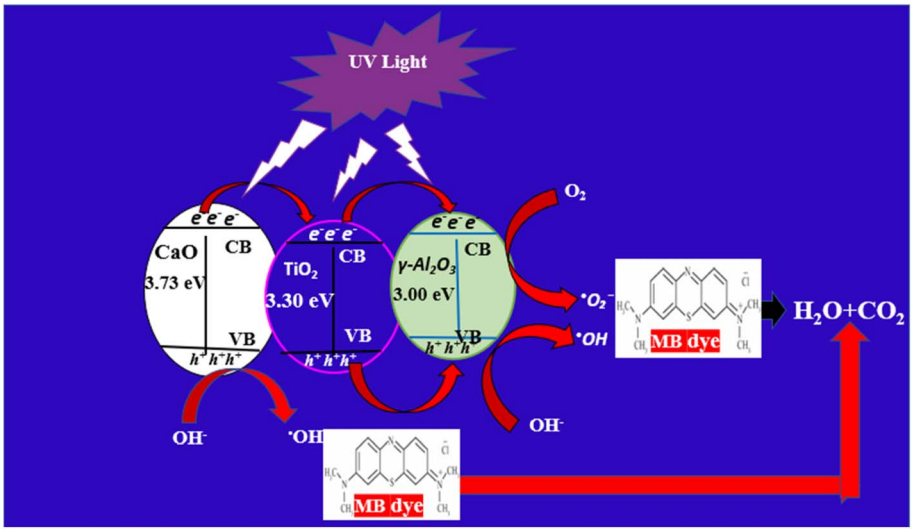

Fig. 10 Possible mechanism of the decomposition of the MB dye using the prepared CaO/TiO_2/γ-Al_2O_3 NCs.

3.8.2 Mechanism of the photodegradation of the MB dye. Fig. 10 describes a schematic representation of the proposed mechanism for the degradation of MB dye using the prepared CaO/TiO_2/γ-Al_2O_3 NCs. There is a different probable mechanism of degradation of the MB dye as follows. Initially, when the NCs are exposed to UV irradiation, the electron in CaO absorbs photons and is excited from the valence band (VB) to the conduction band (CB), as shown in eqn (3). Those electrons (e^-) will then transfer to TiO_2 and are later transferred to γ-Al_2O_3, leaving holes (h^+) that will then transfer to γ-Al_2O_3, as illustrated in eqn (4) and (5). After that, these electrons (e^-) subsequently reduce oxygen molecules to generate superoxide anions $^{\bullet}O_2^-$ and the holes oxide hydroxide ions to form hydroxyl radical $^{\bullet}OH$ as demonstrated in eqn (6) and (7), respectively. Furthermore, these $^{\bullet}OH$ strike the phenol molecules and decompose them down into smaller intermediates, therefore generating compounds such as CO_2 and H_2O, as shown in eqn (8).[62] The reaction process is described in the following equations.

$$\text{CaO/TiO}_2\text{/}\gamma\text{-Al}_2\text{O}_3\text{ NCs} + h\nu \rightarrow \text{CaO/TiO}_2\text{/}\gamma\text{-Al}_2\text{O}_3\text{ NCs } (h^+ + e^-) \quad (4)$$

$$\text{CaO } (e^-) \rightarrow \text{TiO}_2\ (e^-) \quad (5)$$

$$\text{TiO}_2\ (e^-) \rightarrow \gamma\text{-Al}_2\text{O}_3\ (e^-\text{ defect site}) \quad (6)$$

$$\gamma\text{-Al}_2\text{O}_3\ (e^-) + \text{O}_2 \rightarrow {}^{\bullet}\text{O}_2^- \quad (7)$$

$$\gamma\text{-Al}_2\text{O}_3\ (h^+) + \text{OH}^- \rightarrow {}^{\bullet}\text{OH} \quad (8)$$

$$(^{\bullet}\text{O}_2^- \text{ and } {}^{\bullet}\text{OH}) + \text{MB dye} \rightarrow \text{CO}_2 + \text{H}_2\text{O} \quad (9)$$

4. Conclusion

This work successfully fabricated CaO/TiO_2/γ-Al_2O_3 NCs *via* the one-step co-precipitation route with superior photocatalytic activity. The characterization analysis included studies focused on the structural, morphological, optical, and stability of the synthesised samples, and was accomplished using XRD, TEM, SEM, EDX, Raman, FTIR, PL, and DLS spectroscopy. XRD data reveal the enhanced crystallinity structure and phase purity with the addition of CaO and TiO_2 into γ-Al_2O_3 NPs. TEM analysis of the prepared samples shows a spherical shape with less agglomerations of particles and a particle size of 8.21 ± 2.1 nm after the addition of CaO NPs. The percentages of elements (Ca, Ti, Al, and O) in the prepared CaO/TiO_2/γ-Al_2O_3 NCs were confirmed through EDX spectra. The bonds and functional groups within molecules of the prepared samples were determined from Raman and FTIR spectra. Optical properties that determine the recombination of electron–hole pairs are revealed through PL analysis. DLS data show that the average particle distribution of the synthesized γ-Al_2O_3 NPs, TiO_2/γ-Al_2O_3 NCs, and CaO/TiO_2/γ-Al_2O_3 NCs was found to be 190.2 ± 68.1 nm, 180.5 ± 90.3 nm, and 188.2 ± 75.0 nm, respectively. Moreover, the zeta potential of the samples decreased from −11.2 ± 16.6 mV to −28.9 ± 4.3 mV with the addition of the supporting TiO_2 and CaO NPs. Photocatalytic experiments show that under irradiation by UV light for 200 min, the CaO/TiO_2/Al_2O_3 NCs achieved the highest degradation efficiency (98%) of the MB dye compared to the individual samples. These results indicate that the addition of TiO_2 and CaO NPs into γ-Al_2O_3 improved the photocatalytic performance due to their high surface area and promoted charge separation. This study suggests that synthesized CaO/TiO_2/γ-Al_2O_3 NCs can be applied to sustainable solutions in wastewater treatment and other environmental applications.

Data availability

The data in this work are obtained from the corresponding author upon reasonable request.

Author contributions

This work was performed by Emaan Alsubhe.

Conflicts of interest

The authors confirm that the work presented here is original research and has not been submitted for publication elsewhere.

Acknowledgements

The author is grateful for research support from Taibah University.

References

1 C. Martinez-Gómez, I. Rangel-Vazquez, R. Zarraga, G. Del Ángel, B. Ruíz-Camacho, F. Tzompantzi, E. Vidal-Robles and A. Perez-Larios, *Processes*, 2022, **10**(6), 1186.
2 F. T. Li, Y. Zhao, Y. J. Hao, X. J. Wang, R. H. Liu, D. S. Zhao and D. M. Chen, *J. Hazard. Mater.*, 2012, **239–240**, 118–127.
3 A. A. Ismail, I. Abdelfattah, M. F. Atitar, L. Robben, H. Bouzid, S. A. Al-Sayari and D. W. Bahnemann, *Sep. Purif. Technol.*, 2015, **145**, 147–153.
4 J. J. Rueda-Marquez, I. Levchuk, P. Fernández Ibañez and M. Sillanpää, *J. Cleaner Prod.*, 2020, **258**, 120694.
5 M.-J. Zhou, W.-T. Zhang, Z. Li, T. Feng, S. Lan, Z. Peng and S.-Q. Chen, *Rare Met.*, 2023, **42**, 3443–3454.
6 R. Kaveh and H. Alijani, *J. Asian Ceram. Soc.*, 2021, **9**, 343–365.
7 X. Li, H. Zhou, R. Qian, X. Zhang and L. Yu, *Chin. Chem. Lett.*, 2025, **36**, 110036.
8 A. Sridevi, S. Krishnamohan, M. Thairiyaraja, B. Prakash and R. Yokeshwaran, *Inorg. Chem. Commun.*, 2022, **138**, 109311.
9 Z. A. M. Alaizeri, H. A. Alhadlaq, S. Aldawood and M. Ahamed, *Catalysts*, 2024, **14**(12), 923.
10 Z. Alqarni, *Res. Chem. Intermed.*, 2025, 1–24.
11 I. Ahmad, Y. Zou, J. Yan, Y. Liu, S. Shukrullah, M. Y. Naz, H. Hussain, W. Q. Khan and N. R. Khalid, *Adv. Colloid Interface Sci.*, 2023, **311**, 102830.
12 P. Mallick, S. K. Sahoo and S. K. Satpathy, *J. Mol. Liq.*, 2024, **406**, 125071.
13 Z. Cheng, S. Zhao and L. Han, *Nanoscale*, 2018, **10**, 6892–6899.
14 I. Koltsov, G. Kimmel, S. Stelmakh, K. Sobczak and W. Lojkowski, *Sci. Rep.*, 2019, **9**(1), 5540.
15 S. Islak, S. Buytoz, E. Ersoz, N. Orhan, J. Stokes, M. S. J. Hashmi, I. Somunkiran and N. Tosun, *Optoelectron. Adv. Mater., Rapid Commun.*, 2012, **610**, 844–849.
16 D. Oh, Y.-R. Jo, J. Chang, H. An, H. J. Kim, J. M. Vohs, W. Jung and S. Lee, *ACS Appl. Mater. Interfaces*, 2024, **16**, 64714–64724.
17 A. Sridevi, S. Krishnamohan, M. Thairiyaraja, B. Prakash and R. Yokeshwaran, *Inorg. Chem. Commun.*, 2022, **138**, 109311.
18 Y. E. Kim, W. Lee, M. H. Youn, S. K. Jeong, H. J. Kim, J. C. Park and K. T. Park, *J. Ind. Eng. Chem.*, 2019, **78**, 73–78.
19 D. Huang, W. Xie, Z. Tu, F. Zhang, S. Quan and L. Liu, *J. Nanosci. Nanotechnol.*, 2013, **13**(1), 260–269.
20 W. Mahdi, A. Flayyih and F. Musa, *J. Kim. Valensi*, 2024, **10**(2), 277–289.
21 R. Dubadi, E. Weidner, B. Samojeden, T. Jesionowski, F. Ciesielczyk, S. Huang and M. Jaroniec, *Molecules*, 2023, **28**(5), 2002.
22 R. J. Kudla, S. Subramanian, M. S. Chattha and T. E. Hoost, *Ind. Eng. Chem. Res.*, 1996, **35**, 4394–4397.
23 C.-S. Lee, H. Rho, N. Sharma, B. Jung and P. Westerhoff, *ACS ES& T Water*, 2023, **3**(8), 2481–2490.
24 M. Jeevarathinam and I. V. Asharani, *Sci. Rep.*, 2024, **14**(1), 9718.
25 H. Derikvandi and A. Nezamzadeh-Ejhieh, *J. Colloid Interface Sci.*, 2017, **490**, 314–327.
26 A. Kanwal, S. Sajjad, S. A. K. Leghari and M. N. Khan, *Chin. J. Chem. Eng.*, 2021, 147–159.
27 T. Jan, S. Azmat, Q. Mansoor, H. M. Waqas, M. Adil, S. Z. Ilyas, I. Ahmad and M. Ismail, *Microb. Pathog.*, 2019, **134**, 103579.
28 A. M. Rheima, A. A. Anber, H. I. Abdullah and A. H. Ismail, *Nano Biomed. Eng.*, 2021, **13**, 1–5.
29 K. Atrak, A. Ramazani and S. Taghavi Fardood, *J. Mater. Sci.: Mater. Electron.*, 2018, **29**, 8347–8353.
30 S. Mahshid, M. Askari, M. Sasani Ghamsari, N. Afshar and S. Lahuti, *J. Alloys Compd.*, 2009, **478**, 586–589.
31 T. Theivasanthi and M. Alagar, Titanium dioxide (TiO_2) Nanoparticles-XRD Analyses-An Insight, *arXiv*, 2013, preprint arXiv:1307.1091, DOI: 10.48550/arXiv.1307.1091.
32 M. J. Valero-Romero, J. G. Santaclara, L. Oar-Arteta, L. van Koppen, D. Y. Osadchii, J. Gascon and F. Kapteijn, *Chem. Eng. J.*, 2019, **360**, 75–88.
33 T. N. Blanton and C. L. Barnes, Quantitative Analysis Of Calcium Oxide Desiccant Conversion To Calcium Hydroxide Using X-Ray Diffraction.
34 M. Galván-Ruiz, J. Hernández, L. Baños, J. Noriega-Montes and M. E. Rodríguez-García, *J. Mater. Civ. Eng.*, 2009, **21**(11), 694–698.
35 A. Roy and J. Bhattacharya, *Int. J. Nanosci.*, 2012, **11**(5), DOI: 10.1142/S0219581X12500275.
36 Y. Rozita, R. Brydson and A. Scott, 2010.
37 P. Arunarajeswari, T. Mathavan, A. Divya and A. M. F. Benial, *Mater. Res. Express*, 2020, **6**(12), 1250c9.
38 K. Loza, M. Epple and M. Maskos, *Biological Responses to Nanoscale Particles: Molecular and Cellular Aspects and Methodological Approaches*, 2019, pp. 85–100.
39 B. R. Cuenya, *Thin Solid Films*, 2010, **518**(12), 3127–3150.
40 I. Limón-Rocha, A. Marizcal-Barba, C. A. Guzmán-González, L. M. Anaya-Esparza, S. Ghotekar, O. A. González-Vargas and A. Pérez-Larios, *Inorganics*, 2022, **10**(10), 157.
41 A. Esfandyari Bayat, R. Junin, S. Shamshirband and W. Tong Chong, *Sci. Rep.*, 2015, **5**(1), 14264.
42 S. A. Hassanzadeh-Tabrizi, *J. Alloys Compd.*, 2023, **968**, 171914.
43 Y. Q. Cheng and E. Ma, *Prog. Mater. Sci.*, 2011, **56**(4), 379–473.
44 Z. A. M. Alaizeri, H. A. Alhadlaq, S. Aldawood and N. A. Y. Abduh, *RSC Adv.*, 2024, **14**, 16685–16695.
45 M. Mohamad, N. Ngadi, S. Wong, N. Y. Yahya, I. M. Inuwa and N. S. Lani, *Int. J. Eng., Trans. B*, 2018, **31**, 1326–1333.

46 A. P. Naik, H. Mittal, V. S. Wadi, L. Sane, A. Raj, S. M. Alhassan, A. Al Alili, S. V. Bhosale and P. P. Morajkar, *J. Environ. Manage.*, 2020, **258**, 110029.
47 P. Deka, R. C. Deka and P. Bharali, *New J. Chem.*, 2016, **40**, 348–357.
48 Y. Tang, G. Chen, J. Zhang and Y. Lu, *Bull. Chem. Soc. Ethiop.*, 2011, **25**, 37–42.
49 I. González De Arrieta, A. Zaki, A. Canizarès, E. Véron, C. Genevois, L. Del Campo, C. Blanchard and O. Rozenbaum, *Spectrochim. Acta, Part A*, 2023, **298**, 122795.
50 S. Gullapelli, M. S. Scurrell and D. K. Valluri, *Int. J. Hydrogen Energy*, 2017, **42**, 15031–15043.
51 T. Schmid and P. Dariz, *J. Raman Spectrosc.*, 2014, **46**(1).
52 A. H. Gharbi, S. E. Laouini, H. Hemmami, A. Bouafia, M. T. Gherbi, I. Ben Amor, G. G. Hasan, M. M. S. Abdullah, T. Trzepieciński and J. A. A. Abdullah, *Coatings*, 2024, **14**(7), 848.
53 P. Manogar, J. Esther Morvinyabesh, P. Ramesh, G. Dayana Jeyaleela, V. Amalan, J. S. Ajarem, A. A. Allam, J. Seong Khim and N. Vijayakumar, *Mater. Lett.*, 2022, **311**, 131569.
54 R. Gayathri, G. Raja and P. Rajeswaran, *J. Mater. Sci.: Mater. Electron.*, 2020, **31**, 9742–9752.
55 P. A. Prashanth, R. S. Raveendra, R. Hari Krishna, S. Ananda, N. P. Bhagya, B. M. Nagabhushana, K. Lingaraju and H. Raja Naika, *J. Asian Ceram. Soc.*, 2015, **3**, 345–351.
56 Y. X. Zhang, G. H. Li, Y. X. Jin, Y. Zhang and J. Zhang, *Chem. Phys. Lett.*, 2002, **365**(3–4), 300–304.
57 J. Ji, X. Yao, J. Gao, W. Lu, W. Wang and D. Chu, *Chem. Phys. Lett.*, 2021, **781**, 138996.
58 A. Siddiqa, S. Haider, M. Mushtaq, S. Farooq and S. Shahida, *J. Dispersion Sci. Technol.*, 2025, 1–18.
59 A. Noruozi and A. Nezamzadeh-Ejhieh, *Chem. Phys. Lett.*, 2020, **752**, 137587.
60 N. Alomayrah, M. Ikram, S. Alomairy, M. S. Al-Buriahi, M. Naziruddin Khan, M. Farooq Warsi and A. Irshad, *Results Phys.*, 2024, **64**, 107902.
61 N. Almulhem, C. Awada and N. M. Shaalan, *Crystals*, 2022, **12**(7), 911.
62 N. S. Alsaiari, F. M. Alzahrani, A. Amari, H. Osman, H. N. Harharah, N. Elboughdiri and M. A. Tahoon, *Molecules*, 2023, **28**(1), 463.